Chemical Engineering Journal 338 (2018) 72–81

Contents lists available at ScienceDirect

Chemical Engineering Journal

journal homepage: www.elsevier.com/locate/cej

Atomic-layer-deposited TiO_2-SnZnO/carbon nanofiber composite as a highly stable, flexible and freestanding anode material for lithium-ion batteries

Bhavana Joshi[a,1], Edmund Samuel[a,1], Min-Woo Kim[a], Sera Park[a], Mark T. Swihart[b], Woo Young Yoon[c,*], Sam S. Yoon[a,*]

[a] School of Mechanical Engineering, Korea University, Seoul 02841, Republic of Korea
[b] Department of Chemical & Biological Engineering, University at Buffalo, The State University of New York, Buffalo, NY 14260-4200, USA
[c] Department of Materials Science & Engineering, Korea University, Seoul 02841, Republic of Korea

HIGHLIGHTS

- A highly stable, freestanding, and flexible anode material for lithium-ion batteries (LIB) was synthesized into a nanofiber.
- TiO_2 was coated on a SnZnO/carbon nanofiber using atomic layer deposition (ALD).
- Because of the buffering TiO_2 layer, no signs of anode degradation even after 700 cycles.
- These durable and lightweight LIBs should promote the use of ALD in the battery industry.

ARTICLE INFO

Keywords:
Electrospinning
SnZnO
Carbon nanofiber
Atomic layer deposition
Lithium-ion battery
Anode

ABSTRACT

We demonstrate the synthesis of a highly stable, freestanding and flexible anode material for lithium-ion batteries created by depositing a conformal coating of TiO_2 on a SnZnO/carbon nanofiber (CNF) composite using atomic layer deposition. The term SnZnO is used here because metallic Sn is observed in the SnZnO/CNF composites after annealing under argon gas. The elemental composition of the material was confirmed by energy-dispersive X-ray spectroscopy, while the oxidation states of the elements were determined by X-ray photoelectron spectroscopy. Cross-sectional transmission electron microscopy showed that the core regions of the composite nanofibers were almost uniformly covered by a TiO_2 shell. The specific capacities of the TiO_2-coated and uncoated samples at a high current density (5C) were 413 and 159 $mAh{\cdot}g^{-1}$, respectively. An analysis of the surface morphology after cycling indicated that the stability of the solid electrolyte interface layer increased after the formation of the protective conformal TiO_2 layer. As a result, no signs of anode degradation were observed even after 700 cycles at a current density of 5C. We attribute this exceptional stability to the buffering of the anode material by the protective coating during volumetric expansion.

1. Introduction

One-dimensional (1D) nanomaterials, including nanorods, nanowires, nanotubes, and nanofibers (NFs), are garnering attention for use in lithium-ion batteries (LIB) as they allow for greater lithium storage, shorten the carrier transport pathway and buffer the volume expansion of embedded metal oxides [1]. Carbonized NFs (CNFs) are a highly conductive material and eliminate the need for a current collector, resulting in lightweight LIBs [2]. Such NFs can be prepared by several methods. Centrifugal spinning methods use polymer-filled spinnerets and produce fibers by rotating the spinneret to generate the centrifugal force required to overcome the surface tension of the fluid and form a jet that, on elongation, becomes a fiber [3,4]. Forcespinning works on the same principle as centrifugal spinning. However, the fibers can be produced at speeds up to 12,000–25,000 rpm [5,6]. In solution blowing methods, a polymer solution is extruded via a nozzle in a stream of high pressure flowing air that drags the polymer solution into elongated strands that become fibers upon solidification [4]. Electrospinning (ES) involves the use of an electrostatic force and the spinning of the ejected polymer solution [7], with the latter step involving the following three processes: 1) the controllable pumping of the precursor solution, 2) the fine-tuning of the Taylor cone of the liquid jet, and 3) balancing the

* Corresponding authors.
E-mail addresses: wyyoon@korea.ac.kr (W.Y. Yoon), skyoon@korea.ac.kr (S.S. Yoon).
[1] These authors have contributed equally.

https://doi.org/10.1016/j.cej.2018.01.004
Received 19 September 2017; Received in revised form 15 December 2017; Accepted 2 January 2018
Available online 03 January 2018
1385-8947/ © 2018 Elsevier B.V. All rights reserved.

electrostatic force and surface tension of the precursors to obtain uniform CNFs and their composites [4]. Each technique has its own merits and could potentially be utilized for making lithium battery anode materials like those described here. However, CNFs and their composites fabricated by the commercially feasible ES technique show great promise owing to their scalability and well-defined surface morphologies. Particularly for new material development, the controllability of the ES process is a great advantage.

Metal oxides such as Fe_2O_3, MnO and TiO_2, are used with CNFs to form composite electrodes for LIBs through ES because of their high specific capacity [8]. In addition, Sn-based carbon composites are promising anode materials for LIBs because of the high theoretical capacity of SnO_2 (782 $mAh{\cdot}g^{-1}$ after the first cycle) [9], which is more than twice that of commercial graphite anodes (372 $mAh{\cdot}g^{-1}$). Significantly, the theoretical capacity of SnO_2 should be 1494 $mAh{\cdot}g^{-1}$, corresponding to reaction with 8.4 mol of Li ions per Sn atom during the first cycle. This is a unique feature of SnO_2 amongst all the metal oxides [10]. Furthermore, SnO_2 is environmentally friendly, abundantly available, and has a high lithium storage capacity because of its alloying mechanism [11]. However, the volume expansion of tin oxide (300%) results in pulverization, which becomes a significant drawback for Sn-based anodes [12–14]. To address this issue, one can exploit the alloying capability of Sn as an advantage to combine it with zinc so that its volume expansion is alleviated and agglomeration due to pulverization is buffered [15]. Additionally, both Sn and Zn are capable of reversibly alloying with lithium. The combination retains high specific capacity, with up to 7 Li-ions utilized per SnZn pair (4 by Sn and 3 by Zn). However, even though the degree of pulverization is minimized in this manner, the decomposition of the electrode and electrolyte continues, resulting in the formation of a thick solid electrolyte interphase (SEI) layer, which adversely affects the performance of LIBs [16,17]. Further, with continuous charging/discharging, the active oxide material still undergoes contraction/expansion and eventually loses its mechanical integrity. This phenomenon not only causes the pulverization of the oxide material but also leads to breakage of the SEI layer, decreasing the cycling performance [17].

Therefore, surface modification of LIB electrodes is a powerful approach for ensuring that the SEI layer formed is thin and stable [18]. The atomic layer deposition (ALD) method can be used to form pinhole-free, ultrathin, and conformal coatings on surfaces with complex topographies, providing control of the SEI formation process through surface passivation [19,20]. Several studies have demonstrated that the electrochemical performance of cathodes of $LiMn_2O_4$ and $LiCoO_2$ and anodes of graphene, Si, and Fe_2O_3 can be improved through surface modification with an ALD coating [21–27]. This surface modification technique has also been used with SnO_2 anodes, on which thin coatings of $HfO_2/TiO_2/Al_2O_3$ have been formed by ALD [26,28,29]. However, the passivation of freestanding and flexible CNF composite anodes by ALD has not yet been explored.

The surfaces of composite fibers are usually modified by coating them with a thin passivating layer of TiO_2, in order to ensure higher stability and to prevent the decomposition of the electrolyte and electrode [24,26]. TiO_2 coatings are electrochemically stable and ionically conductive and thus allow for ready charge transfer. Moreover, TiO_2 exhibits a volume expansion on lithiation of less than 4% and is known for its high safety [30]. To the best of our knowledge, the stability of SnZnO CNFs passivated by an ALD-TiO_2 layer has not yet been studied. In this paper, we report the effects of TiO_2 coatings of different thicknesses on SnZnO CNFs on the properties of the fibers. A TiO_2 layer of optimal thickness improved the stability of the composite at high current densities. Further, an analysis of the post-cycling surface morphology of the composite indicated that the mechanical strength of the SEI layer was improved by the ALD-TiO_2 coating.

2. Experimental

2.1. Electrospinning process

The SnZnO NFs were prepared by mixing 3 wt% tin(II) acetate (SnAc, $Sn(CH_3CO_2)_2$, Sigma-Aldrich) and 1 wt% zinc acetate dihydrate (ZnAc, $Zn(CH_3COO)_2{\cdot}2H_2O$, 98%, Sigma-Aldrich) in an 8 wt% polyacrylonitrile (PAN, MW = 150 kDa, Sigma-Aldrich) and N,N-dimethylformamide (DMF, 99.8%, Sigma-Aldrich) solution. The mixture was stirred for 24 h at room temperature to form a homogeneous solution. The SnAc-ZnAc/PAN-DMF solution was then injected from two syringe pumps at a flowrate of 250 µl/h and electrospun onto a drum collector rotating at 200 rpm. The voltage was adjusted to 7.8 kV, in order to ensure a stable Taylor cone. Further, the NFs were stabilized at 280 °C for 30 min using a ramping rate of 5 °C/min. Next, the fibers were carbonized at 700 °C for 1 h in an argon environment using a ramping rate of 3 °C/min. This resulted in flexible, freestanding and conductive SnZnO CNFs.

2.2. TiO_2 coating by ALD process

To form the passivating TiO_2 coating, the flexible and freestanding fibers were placed in the ALD system. The alkoxide precursor titanium isopropoxide (TTIP) was used as the Ti source for TiO_2 deposition owing to its high vapor pressure, non-corrosive nature, and self-limiting growth, factors that result in high-purity coatings. H_2O was used as the oxidizing agent for the surface reactions.

The TiO_2 ALD reaction was performed through the static exposure of the fibers to TTIP and H_2O in the ALD reactor. The TTIP precursor was delivered into the vacuum chamber using N_2 as the carrier gas. The temperature of the bubbler and delivery line were maintained at 76–78 °C to prevent the condensation of TTIP. The reaction was carried out in three steps: 1) TTIP was pulsed for 1 s, followed by a 20 s purge with N_2; 2) H_2O was pulsed for 0.3 s, followed by a N_2 purge of 10 s to evacuate the reaction products and excess TTIP; and 3) finally, during the post-deposition process, N_2 was purged for 5 min (300 s). N_2 was used at a flow rate of 50 sccm as both the purging gas and the carrier gas. The chamber pressure during the pulsing of TTIP and H_2O was 925 and 675 mTorr, respectively. The thickness of the TiO_2 layer was controlled by varying the number of iterations of steps 1 and 2, with the TiO_2 deposition rate being 0.1 nm/cycle at 200 °C on a flat surface. It is important to note that due the internal spaces and depth of cylindrical shaped carbon nanofiber composite the total area for conformal coating with TiO_2 by ALD may increase drastically. The samples corresponding to 0, 35, 50 and 75 cycles are labeled as SZT0, SZT35, SZT50 and SZT70, respectively. Fig. 1 shows the steps involved in the fabrication and passivation of the TiO_2-SnZnO CNFs (hereafter referred to as SZT CNFs) as well as a cross-sectional view of a coated CNF showing the TiO_2 coating.

2.3. Physicochemical characterization

X-ray diffraction (XRD) analysis (SmartLab, Rigaku) was used to characterize the crystalline structure of the composite fibers. The surface morphologies of the composite fibers were evaluated using field-emission scanning electron microscopy (FESEM; S-5000, Hitachi, Ltd.) and transmission electron microscopy (TEM; JEM 2100F, JEOL Inc.). The TEM samples were prepared by slicing the fibers with a focused ion beam (FIB, 5nA, LYRA3 XMH, TESCAN); this allowed for cross-sectional imaging. An energy-dispersive X-ray spectrometer with SEM and TEM attachments was used to determine the elemental contents and their distributions. Confocal Raman spectrometry (Jasco, NRS-3100) was used to analyze the carbon content and carbon defects in the mats of the

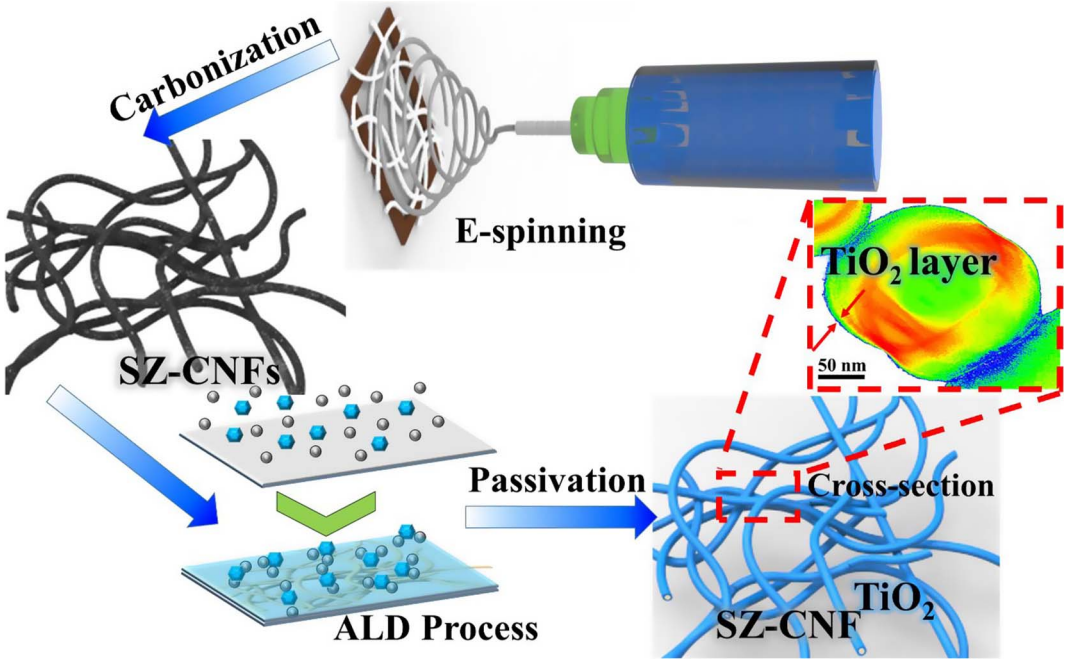

Fig. 1. Schematic of electrospinning and carbonization of SnZnO nanofibers (SZ CNFs), ALD deposition of TiO_2 coating on SZ CNFs and cross-section of SZT CNF.

CNFs (see description below). The chemical states of the elements were determined by X-ray photoelectron spectroscopy (XPS; Theta Probe Base System, Thermo Fisher Scientific Co.). Thermogravimetric analysis (TGA; SDT Q600, TA Instruments) of mats was carried out with a heating rate of 10 °C /min in air.

2.4. Electrochemical characterization

The freestanding CNFs without and with an ALD coating were punched into 1.54 cm^2 discs. The area density of each sample was approximately 0.9 $mg{\cdot}cm^{-2}$. The punched disc samples were used directly as anodes, without any current collector or binder. The electrochemical performance of these disc-like samples was measured using CR2032 coin-type half-cells, in which the reference electrode was a sheet of metallic Li (16 mm in diameter) and the punched mat to be tested was used as the working electrode. A microporous polymer sheet (Celgard 2400; Celgard, Chungbuk, South Korea) was used as the separator. The liquid electrolyte in the cell consisted of 1 M $LiPF_6$ in a solvent mixture of ethylene carbonate, dimethyl carbonate, and ethyl methyl carbonate (1:1:1 by volume) (PuriEL, Soulbrain, Seongnam, South Korea). The electrochemical properties of the of the TiO_2-SnZnO CNFs were investigated through galvanostatic charge/discharge measurements performed using a WBCS3000 battery cycler system (WonATech, Seoul, South Korea) at 25 °C for voltages of 0.005–3 V. The cells were subjected to rate tests at current densities of 0.1C, 1C, 2C, and 5C, where 1C = 1000 $mA{\cdot}g^{-1}$.

3. Results and discussion

3.1. Material properties

The carbonized composite NFs were coated with a conformal layer of TiO_2. The thickness of the deposited TiO_2 coating was tuned at the monolayer-scale by adjusting the number of ALD cycles performed. SnZnO composite particles were embedded within the NFs, as evidenced by the smooth surface morphology of the samples as shown later in Fig. 4b–d. Nonetheless, particles near the surface may form an SEI and undergo pulverization during long-term cycling. In contrast, in the case of the ALD-coated composite NFs, the SEI remained stable and the electrode remained intact.

The formation of the SnZnO CNFs was confirmed by XRD analysis, as shown in Fig. 2a. Peaks related to crystalline ZnO or metallic Zn are not observed in the XRD patterns, owing to their low concentrations. Further, the carbonization in an argon environment reduced the tin oxide, resulting in high-intensity Sn-related peaks. The sharp peaks at 30.64°, 32.03°, 43.8°, 45.02°, 55.3°, 62.5°, 63.78°, 64.5°, 72.4°, 73.19°, and 79.47° correspond to the (2 0 0), (1 0 1), (2 2 0), (2 1 1), (3 0 1), (1 1 2), (4 0 0), (3 2 1), (4 2 0), (4 1 1), and (3 1 2) planes of metallic Sn (JCPDS 04-0673). This phase was attributable to the carbothermal reduction of Sn^{4+} ions to Sn^{2+} and then to Sn^0 by the carbon layer during the high-temperature treatment. No peaks related to TiO_2 were present in the XRD patterns of SZT35, SZT50, and SZT70. The deposited TiO_2 may be amorphous because of the low-temperature deposition process. However, with an increase in the number of TiO_2 coating cycles, the intensity of the Sn peaks decreased, suggesting an increase in the thickness of the TiO_2 layer. A broad hump at approximately 22–27° was observed for all the cases and was attributed to the carbon of the CNFs.

Further, the composite samples were characterized by Raman spectroscopy to confirm the presence of graphitic and defective carbon in the composite NFs. The bands observed at 1348 and 1586 cm^{-1} (see Fig. 2b) correspond to disordered (*D* band, sp^3 bonding) and graphitic carbon (*G* band, sp^2 bonding), respectively, and were present in the case of every sample. The intensity of the *D* band (I_D) was greater than that of the *G* band (I_G) for all the cases, indicating that a large number of defects were present in the composite NFs. Such defects allows diffusion of Li ions and provide intercalation sites for Li, resulting in enhanced Li storage. Such defect activated storage is expected to result in enhanced reversible capacity as explained by Lichit et al. [31]. In general, increasing the carbonization temperature reduces the defect concentration and improves the graphitization of CNFs. However, high carbonization temperature allows the metal particles to agglomerate after their reduction, which further degrades the electrochemical performance of the composite fiber electrode. Further, we expect that the disordered nature of the NFs as well as the defects within them would allow for the nucleation and growth of metal oxide particles [32].

The morphologies of the ALD-coated SnZnO CNFs were studied in

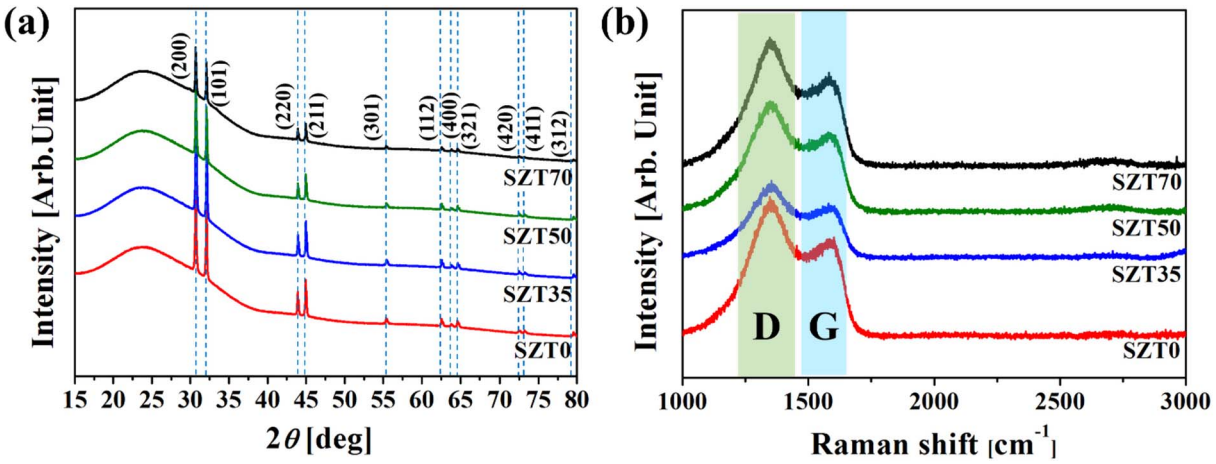

Fig. 2. (a) XRD patterns and (b) Raman spectra of SZT0, SZT35, SZT50 and SZT70 composite NFs.

detail by TEM. As mentioned above, cross-sectional TEM samples were obtained using the FIB technique. The results are shown in Fig. 3. The presence of crystalline Sn in the fibers is confirmed by the fringes observed in the HRTEM image. The *d*-spacings between two parallel lattice fringes are 0.29 and 0.27 nm, which correspond to the (2 0 0) and (1 0 1) planes of Sn (JCPDS 04-0673), respectively. Further, the distinct contrast of the 2.2-nm-thick TiO_2 layer on SZT50 shows that the NFs were well coated with an amorphous TiO_2 layer (see Fig. 3b). As the ALD coating rate was 0.1 nm/cycle for a flat surface, 50 cycles would produce a 5 nm thick coating on a flat surface. However, for the mat of cylindrical CNFs with internal spaces, as observed in Fig. 4b–d, the deposition rate was lower. From HRTEM imaging, the TiO_2 conformal coating thickness corresponds to a deposition rate of ~0.044 nm/cycle on the fibers. Thus, the probable thickness of TiO_2 for SZT35 and SZT70 could be ~1.54 and 3.1 nm for 35 and 70 cycles of TiO_2 respectively. Furthermore, at low temperatures, ALD results in the deposition of amorphous TiO_2, which can undergo crystallization if the number of cycles is increased to more than 200, depending on the growth rate per cycle, as reported by Guerra-Nunez et al. [33]. With only 50 cycles performed in this study, amorphous TiO_2 was observed, in keeping with the above-mentioned report. The thickness of TiO_2 layer over SnZnO fiber after 35 (SZT35) and 70 (SZT70) cycles is shown in Fig. S1.

The elemental maps of the composite NFs, shown in Fig. 4a, confirm that the primary constituent elements were C and Sn. Further, Zn was also present along with Sn and Ti over the entire surface of the SnZnO CNFs, forming a shell-like covering. The presence of Ti in the central region may be attributable to the diffusion of Ti atoms through paths within the porous electrode, which also ensured the conformal deposition of TiO_2 over the entire electrode structure [28]. Further, the morphology of the SnZnO CNFs after they had been coated with TiO_2 was examined by SEM; the results are shown in Fig. 4b–d. Histograms showing fiber diameter distributions are presented in Fig. S2. In addition, the results of an elemental analysis of the surfaces of the different SZT samples as determined by EDX/SEM are presented in Table 1. These results clearly show that the Ti concentration increased with increasing number of coating cycles.

XPS measurements were performed to elucidate the surface chemical compositions of the various samples before and after the TiO_2 coating process using ALD. Fig. 5a is the XPS survey spectrum that shows the C, N, O, Sn and Zn signals. Further, Fig. 5b and c show that Ti peaks were present in the survey spectrum after the ALD process. The core Ti 2p spectra (Fig. 5d) of the samples contain two distinct peaks, at 458 and 464 eV; these are ascribed to Ti $2p_{3/2}$ and Ti $2p_{1/2}$ with an energy difference of 6 eV. This energy gap between the Ti 2p peaks indicates that Ti exists as Ti^{4+} in the coatings. It also indicates that the ALD coatings were fully oxidized. The high-resolution spectra for the other elements are given in Fig. S3. The core Sn spectra (Fig. S3a) contain two peaks at 486.7 and 495.1 eV; these can be assigned to Sn

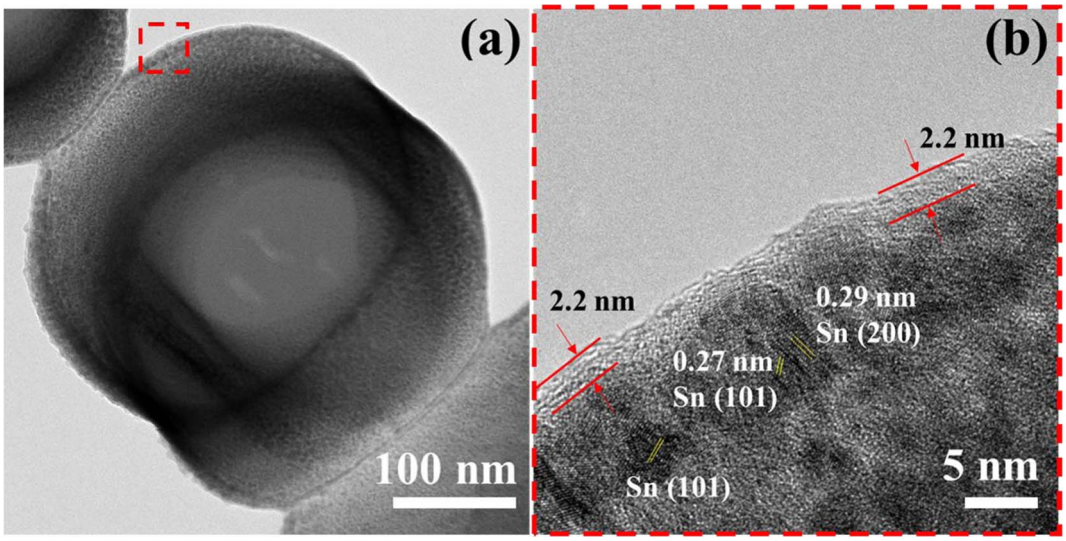

Fig. 3. (a) TEM image of SZT50 and (b) HRTEM image of area marked by red square in (a). (For interpretation of the references to color in this figure legend, the reader is referred to the web version of this article.)

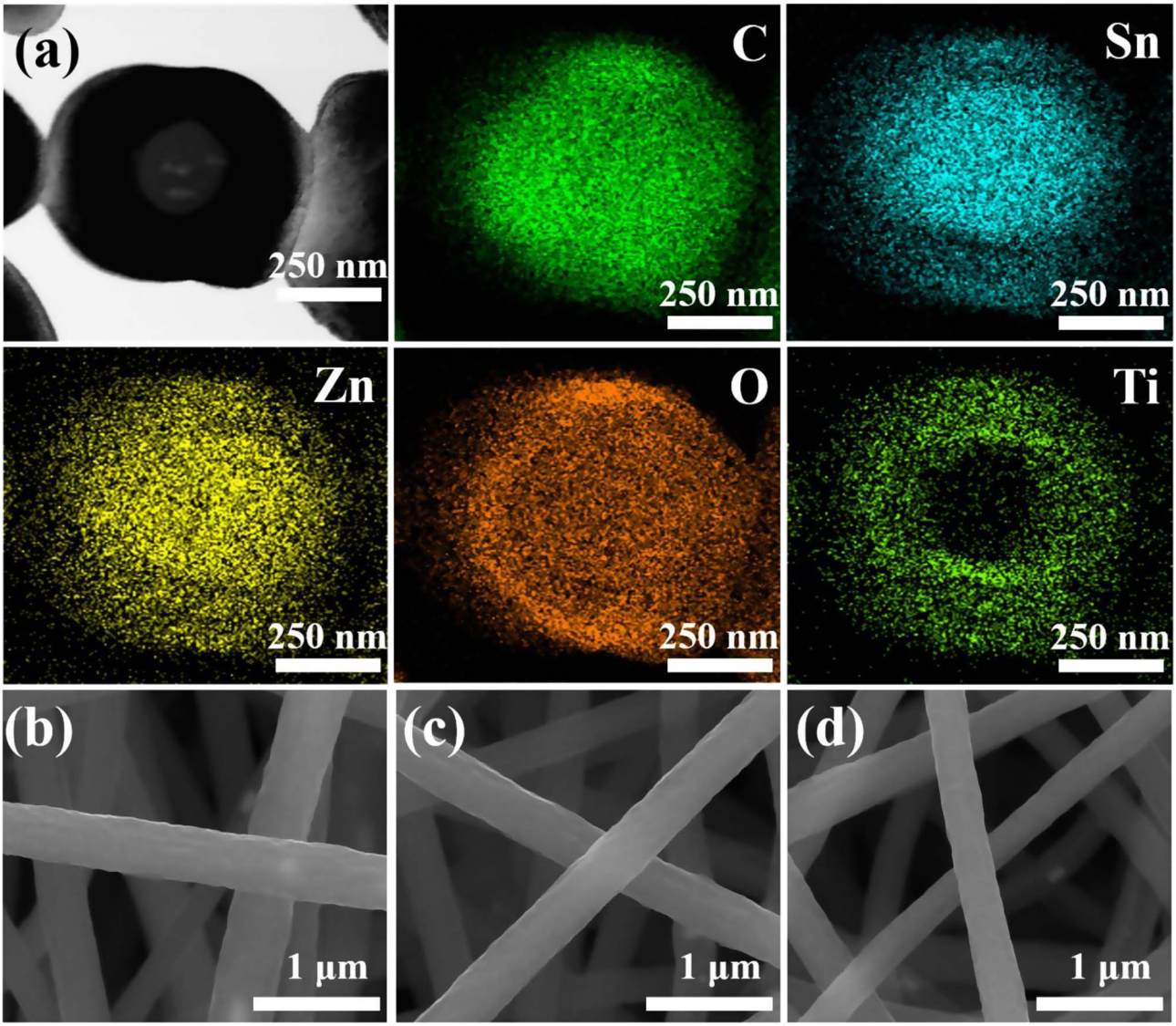

Fig. 4. (a) TEM image of SZT50 and corresponding elemental maps. SEM images of (b) SZT0, (c) SZT50 and (d) SZT70.

Table 1
Elemental compositions of various composites (at%) as determined by EDX.

Elements	SZT0	SZT35	SZT50	SZT70
Sn L	6.3	5.8	6.3	4.9
Zn L	3.3	3.1	3.6	2.8
N K	16.3	16.4	15.1	16.8
C K	55.7	53.8	51.8	52.2
O K	18.5	20.5	22.7	22.3
Ti K	0	0.3	0.6	1.2

$3d_{5/2}$ and Sn $3d_{3/2}$, respectively. The appearance of the Sn peak at 486.7 suggests that Sn was present in the + 4 oxidized state. The peaks at binding energies of 1021.4 and 1045 eV in Fig. S3b correspond to Zn $2p_{3/2}$ and Zn $2p_{1/2}$, respectively. These results confirm that SnO_x and ZnO coexisted in the samples. Peaks were also observed at 285 and 531 eV in the C 1 s and O 1 s spectra, as shown in Figs. S3c and d respectively.

3.2. Electrochemical performance

The galvanostatic discharging (lithiation)/charging (delithiation) curves of the half cells produced using the composite samples subjected to different numbers of ALD cycles are presented in Fig. 6. The lithiation curves exhibit different regions related to the insertion of Li in the composites. The rapid drop in the voltage until 1.2 V and the subsequent moderate drop up to 0.7 V correspond to the initiation of Li insertion in the CNFs. Further, the long slope-like section extending from 0.7 to 0.005 V corresponds to the insertion of Li^+ ions in SnZnO and the formation of their alloys, which resulted in a capacity of approximately 1300 $mAh{\cdot}g^{-1}$. These characteristic voltages are well supported by cyclic voltammetry (CV) measurements as discussed and shown in supporting information Fig. S4. For all the electrodes, the lithiation/delithiation processes can be described by the following reactions.

$$SnO_x + 2xLi^+ + 2xe^- \rightarrow Sn + xLi_2O \quad (1)$$

$$Sn + xLi^+ + xe^- \leftrightarrow Li_xSn (0 < x < 4.4) \quad (2)$$

$$ZnO + 2Li^+ + 2e^- \rightarrow Li_2\ O + Zn \quad (3)$$

$$Zn + xLi^+ + xe^- \leftrightarrow Li_xZn (0 < x < 1.0) \quad (4)$$

Furthermore, the formation of Sn and Zn in the CNFs enhanced the reversible capacity of the electrodes through a synergistic effect. The SZT0, SZT35, SZT50 and SZT70 samples exhibited initial discharge capacities (lithiation) of 1992, 1991, 2096 and 1729 $mAh{\cdot}g^{-1}$,

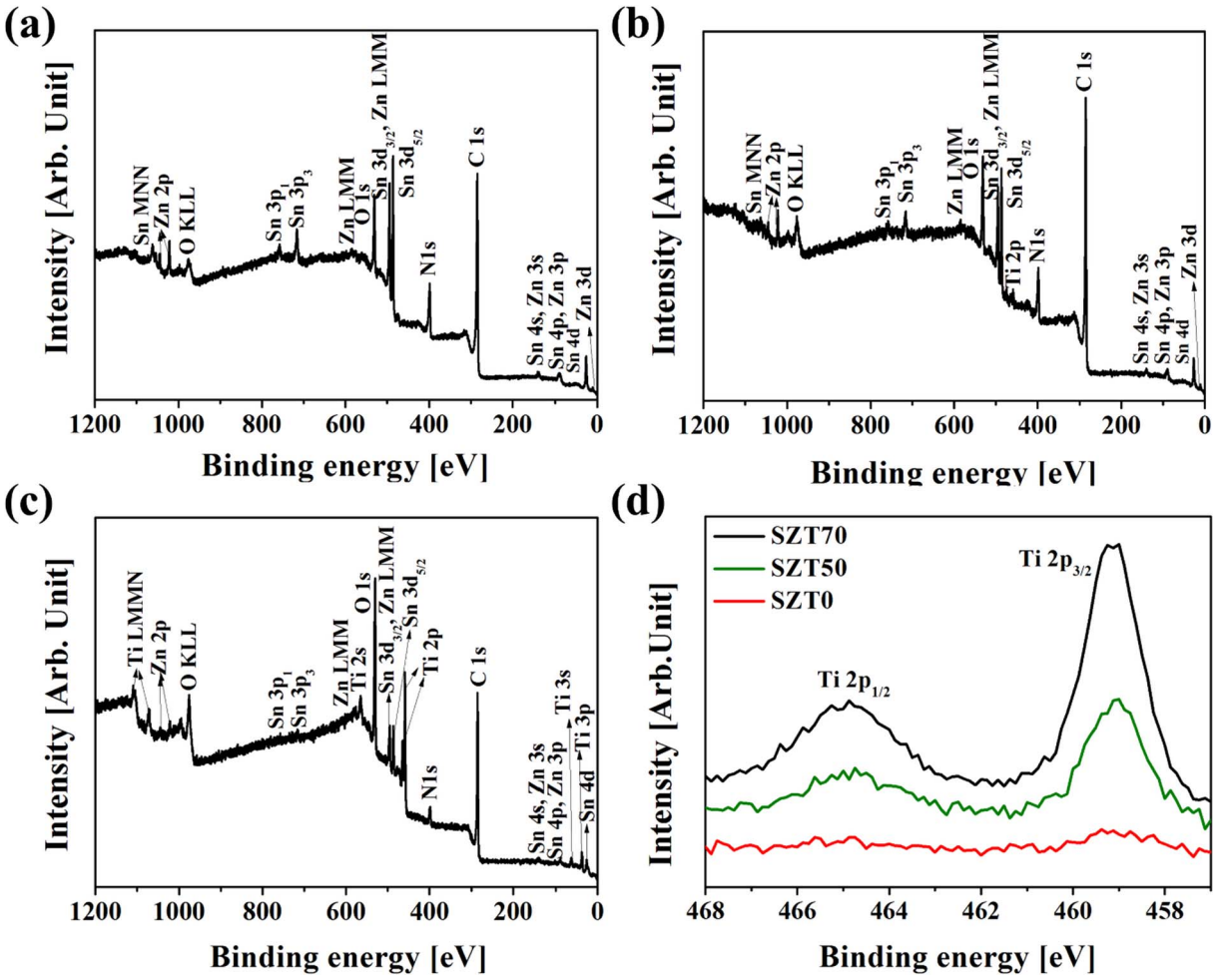

Fig. 5. XPS spectra of (a) SZT0, (b) SZT50, (c) SZT70 and (d) their core Ti 2p spectra.

respectively, at a current density of 0.1C. The specific capacities of the electrodes were calculated based on the total weight of the composite NFs. The plateau-like region between 0.005 and 3 V in the charging curve (delithiation) is related to the reversible reactions described above. However, loss in capacity after delithiation is observed due to SEI formation via decomposition of the electrolyte solution by reaction with Li. The irreversible capacity due to SEI formation observed after the first cycle is similar to the behavior of various other metal oxide/carbon anodes. The first cycle Coulombic efficiency (CE) values of the four composite samples were 68, 76, 73, and 70% for SZT0, SZT35, SZT50, and SZT70, respectively. This improvement in the CE upon TiO_2 coating suggests that the formation of the SEI was mitigated by the passivating layer of ALD TiO_2 on the composite NFs. The relative decrease in the CE of SZT70 was probably ascribable to the consumption of Li ions by TiO_2, which is a low-capacity material. The discharge/charge profiles of the samples indicated similar lithium insertion/extraction processes, owing to their similar elemental compositions. However, the variations in the capacities of the samples and their retention rates clearly reflected the effect of the thickness of the deposited TiO_2 layer. The CE value increased from the second cycle onwards to more than 96% and subsequently became 98%.

The lithiation/delithiation processes occurring within the fabricated anodes and the effect of the passivating TiO_2 layer were explored based on the differential capacities of the anodes. Fig. 7a shows the changes in the differential capacity during discharging for $N = 1$ and 2 cycles. All the samples show three major peaks. However, for each case, the capacity (intensity) decreases with the voltage. The peak potentials indicate that a reaction involving Li ions and Sn occurred, yielding LiSn (~0.61 V). Further, LiSn gradually formed Li_7Sn_2 at ~0.42 V. Sengupta et al. [34] suggested that this multistep transformation of the Li-Sn alloy reduces the volumetric strain as well as the degree of pulverization. The dominant peak at approximately 1 V seen in all the cases vanished during the second discharging cycle, as can be seen from Fig. S5. This clearly marks the completion of the formation of the SEI layer. In addition, the broad peak at 0.5–0.7 V is indicative of a reaction between Li ions and Zn; this is a redox reaction of ZnO and leads to the alloy Zn_xLi_y [32]. A comparison of the differential capacities of the various samples after $N = 1$ cycles shows that there was no significant shift in the peaks or variations in the peak intensities; this was indicative of the effect of the TiO_2 coating. Furthermore, the variations in the differential capacity of each electrode during the charging cycle are shown in Fig. 7b. The results show that the alloying and dealloying of LiSn are highly reversible processes. In addition, a comparison of the intensities of the peaks in the cases of SZT35 and SZT50 with those for SZT0 suggests that the dealloying of Li_xSn_y is enhanced owing to the extent of reversibility of the process being higher, probably owing to the presence of a thinner SEI layer. However, the intensity of the peaks for SZT70 is lower than that for SZT0, confirming that a thick TiO_2 layer hindered the transfer of Li ions owing to which the alloying and dealloying of Li_xSn_y occurred less readily during the lithiation and delithiation stages. This assumption is well supported by the lower capacity values exhibited by SZT70, as shown in Fig. 8.

The results of the lithiation/delithiation measurements performed for current densities ranging from 0.1C to 5C over 90 cycles are presented in Fig. 8. The SZT0 and SZT50 composite electrodes show specific capacities of 1043, 533, 318, and 159, and 1285, 832, 671, and

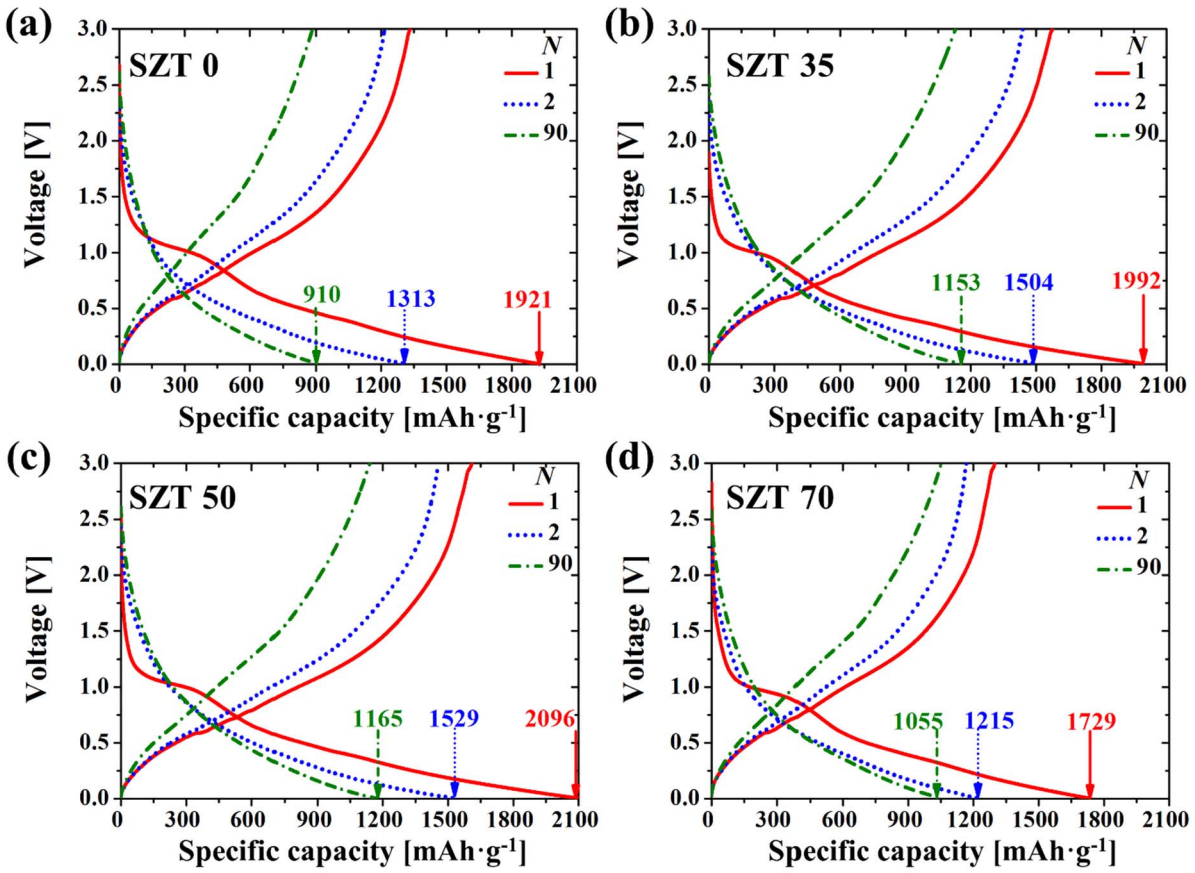

Fig. 6. Discharge/charge profiles of (a) SZT0, (b) SZT35, (c) SZT50 and (d) SZT70.

413 mAh·g^{-1}, respectively, for current densities of 0.1, 1, 2, and 5C. The capacity of the SZT50 composite electrode is 2.6 times higher than that of the uncoated composite electrode at a high current density (i.e., at 5C). When the current density was reduced to 0.1C, the capacities of all the samples returned to their initial values. However, the capacity of SZT0 declined slightly between the 81st and 90th cycles, while the TiO_2-passivated composite NFs exhibited an almost flat curve during the same cycling period. The SZT35 and SZT50 composite electrodes exhibited similar performances at lower current densities of 0.1C and 1C. However, at higher current densities of 2C and 5C, SZT50 showed superior electrochemical stability owing to the presence of an optimized TiO_2 coating. The SZT70 composite electrode showed better performance at 0.1C. However, at a higher current density, it showed poorer performance than that of SZT0. This decrease in the capacity of SZT70 at a higher current density of 5C is attributable to the consumption of a large number of Li ions by TiO_2, owing to which the composite could not deliver a specific capacity greater than its theoretical capacity of 335 mAh·g^{-1} [35]. In addition, the thick TiO_2 layer present probably prevented the deep diffusion of the Li ions. Hence, an insufficient number of Li ions reached the Sn/Zn interface for the electrochemical redox reactions. As mentioned earlier, the coulombic efficiency values of the four composite samples presented in Fig. 8 were determined to be 68, 76, 73, and 70%, respectively after first cycle. However, the CE value increased to 96% from the second cycle

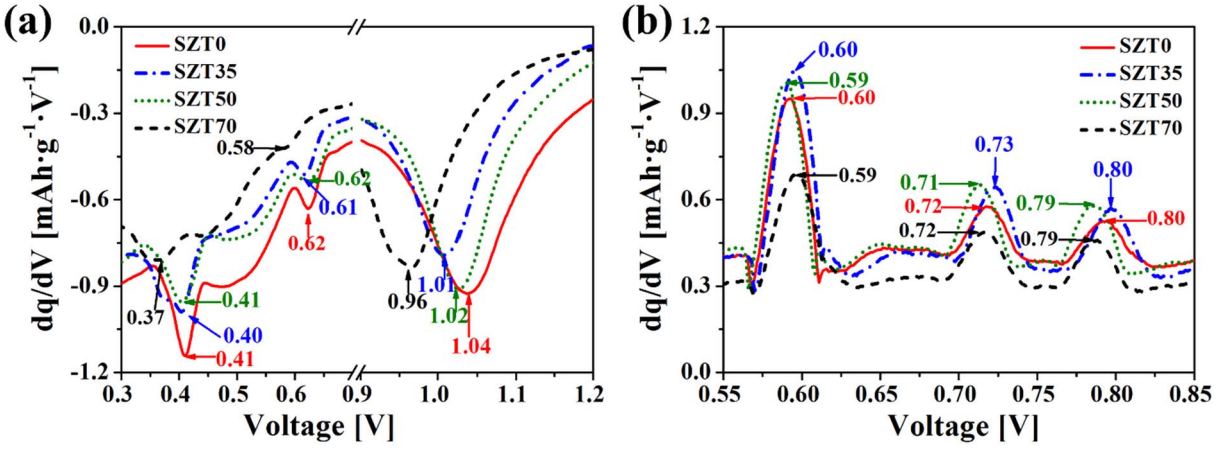

Fig. 7. Differential capacities of various SZT anodes: (a) discharging and (b) charging.

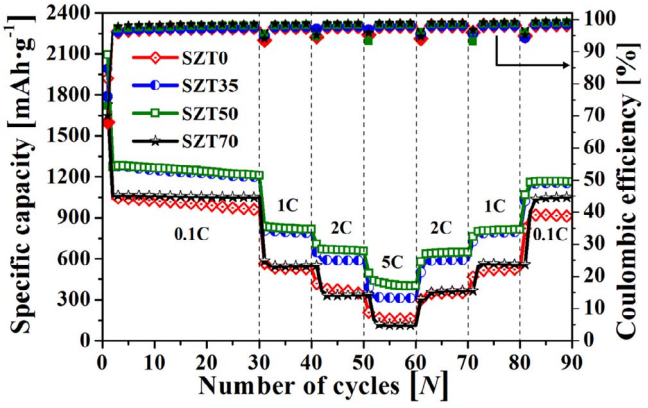

Fig. 8. Rate capabilities and coulombic efficiency of various samples for voltage of 0.005–3.0 V.

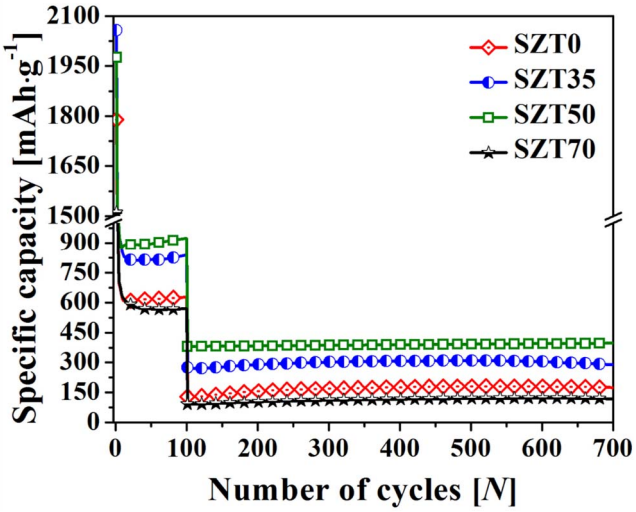

Fig. 9. Long-term cycling performances of various samples at high current density.

onwards. After 90 cycles, the CE values were 96, 97, 98 and 99% for SZT0, SZT35, SZT50 and SZT70 respectively.

The SZT composites were tested for 700 cycles in three stages: (1) at a low current density of 0.1C (N = 1–3), (2) at a high current density of 1C (N = 4–100), and (3) at very high current density of 5C (N = 101–700); this was done to evaluate their long-term stability. The presence of carbon significantly shortens the pathway for ion diffusion and increases the charge transfer rate due to better conductivity. Additionally, CNF intercalates Li as LiC_6, with a theoretical capacity of 479 mAh·g^{-1} and buffers the volume expansion of the SnZnO to realize high and stabilized specific capacity. The performance of the CNF for long-term stability and high current rate capability are demonstrated under various conditions in our previous work [36]. Additionally contributions of CNF, SnZnO and TiO_2 were determined by TGA as shown in Fig. S6 along with estimation of capacity presented in Table S1. Further, the SnZnO/CNF exhibited excellent long-term stability, with composite SZT50 showing the highest capacity of 400 mAh·g^{-1} after 700 cycles at a current density of 5C. This suggested that the optimal number of ALD cycles for depositing the TiO_2 layer is 50, as it resulted in a TiO_2 layer that allowed for the control of the SEI layer thickness and mechanical strength, such that the SEI layer could bear the strain generated, without negatively affecting the specific capacity of the composite NFs. The capacities of samples SZT35 and SZT0 decreased after 600 cycles. However, samples SZT50 and SZT70 showed stable cycling performance. Further, the cycling performance of SZT70 was better than that of SZT0 in terms of stability; however, the latter showed a very low capacity. These results highlight the effect of the passivating TiO_2 coating formed by ALD in enhancing the overall electrochemical performance of the composite NFs, resulting in improved specific capacity, high-current durability, and long-term cycling stability. Furthermore, Table 2 shows that the composite electrodes fabricated in this work exhibited superior performance in terms of the current density and long-term stability as compared to other ALD-passivated Sn-based LIB anodes.

Electrochemical impedance spectroscopy (EIS) is a suitable tool for evaluating the electrochemical impedance at the various junctions between the electrode and the electrolyte. Three main parameters could be extracted from the Nyquist plots of the various composites as determined by EIS; (a) a solution resistance (R_s – initial real-impedance value), (b) a charge-transfer resistance (R_{ct} – intercept of the real-impedance axis), and (c) the diffusion probability based on the Warburg regime (straight line at the tail of the semicircular arc). Solution resistance is associated with the electrode's conductivity, thus the low solution resistance R_s could be attributed to the conductive network of CNF that enables easy electrolyte accessibility and due to shorter Li-ion diffusion pathway [37]. In addition, a low R_{ct} may minimize electrolyte and electrode decomposition by allowing for the ready movement of the Li ions. It also limits the corrosion of the CNFs to a large extent. The presence of a Warburg impedance in the lower-frequency region suggested that SZT50 allowed for Li-ion diffusion to a greater degree than did the other electrodes, as shown in Fig. 10. Although SZT35 showed a lower charge-transfer resistance, in its case, the Warburg regime had a smaller slope than that in the case of SZT50. Thus, the EIS results confirmed the superior electrochemical performance of SZT50 and were in keeping with its high specific capacity and long-term stability, as shown in Fig. 9.

3.3. Post-cycled microstructure

To evaluate the stability of the TiO_2-coated composite CNFs during long-term cycling, the surface morphologies of the electrodes were studied after N = 2 and 700 cycles using SEM. For better visualization, MATLAB-processed SEM micrographs of SZT0 and SZT50 after being cycled at 0.1C for 2 cycles are shown in Fig. 11a and b, respectively. The corresponding original grayscale SEM images are presented in Fig. S7. Additionally, the color bar was added to highlight the SEI layer thickness for easier interpretation of the SEM images. The SZT0 and

Table 2
Comparison of properties of Sn-based electrodes coated with thin metal oxide layer by ALD.

Material/Coating method	ALD coating (N)	First cycle capacity [mAh·g^{-1}]@ current density [mA·g^{-1}]	Capacity [mAh·g^{-1}]@current density [mA·g^{-1}]	Retention capacity [mAh·g^{-1}]@current density [mA·g^{-1}] (N)
SnO_2-rGO/Hydrothermal [28]	HfO_2 (6)	1989@150	500@1500	853@150 (100)
SnO_2 nanowire/ Vapour deposition [29]	*TiO_2 (10 nm)	1421@200	241@3200	494@400 (500)
SnO_2-graphene[38]	Al_2O_3 (10)	2209@100	329@2000	1176@100 (60)
SnO_2 nanocrystal [26]	Al_2O_3 (2)	2400@50	420@1000	883@50 (60)
SnZnO-CNF/electrospinning	*TiO_2 (50)	2100@100	413@5000	400@5000 (700)

* Flexible and freestanding electrodes.

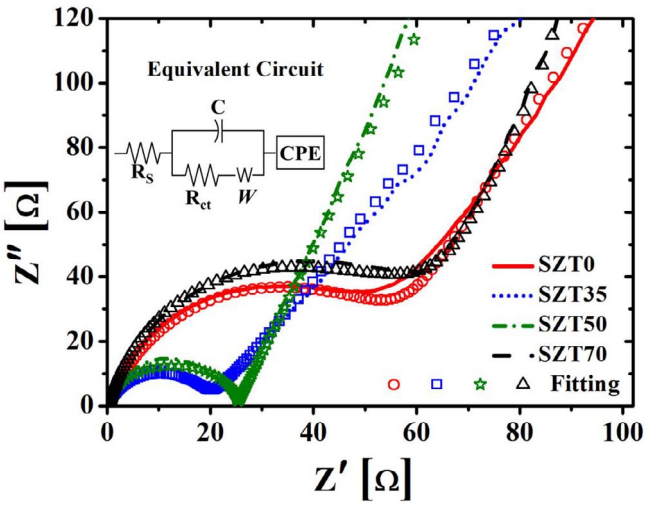

Fig. 10. EIS curves of various SZT CNF composites.

SZT50 anodes clearly exhibit distinct morphologies, confirming that the passivation layer is beneficial for improving the electrochemical performance. For instance, it is evident from the post-cycling microstructural images that the TiO_2 coating formed after 50 ALD cycles retarded the decomposition of the electrolyte and prevented the core composite NFs from decaying. Therefore, an SEI layer with a lower thickness (lighter-blue region over the fiber in Fig. 11b) was formed on the coated composite CNFs after two cycles. On the other hand, the uncoated composite CNFs are relatively dark blue. However, regardless of the surface morphology of the composite NFs, a uniform SEI layer was not observed on them (see Fig. 11a).

Fig. 11c–d show the surface morphologies of SZT0 and SZT50 after 700 cycles. As mentioned earlier, these electrodes had been subjected to $N = 3$ cycles at a current density of 0.1C, $N = 97$ cycles at 1C, and the remaining $N = 600$ cycles at 5C. The surface SEM image of SZT0 reveals that a thick SEI layer was formed on the CNFs and that they underwent a high degree of deformation because of volumetric expansion/contraction. Owing to this deformation, the SEI layer broke, with the new SEI layer consuming Li ions and causing the decomposition of the electrolyte because of the irreversible electrochemical reactions involved. Some of the broken zones of the SEI layers are marked with circles in Fig. 11c. However, no such broken zones were observed in SZT50 even after 700 cycles, as can be seen from Fig. 11d. In addition, the arrow in Fig. 11c points to a region with multiple shades, confirming that multiple SEI layers were formed during the long-term cycling process. On the other hand, the arrow in Fig. 11d points to a region with almost a single color, suggesting that the SEI layer on the fibers of this sample did not break to the same extent and that there was no loss of Li ions or the decomposition of the electrolyte. One can also see that the fibers of SZT50 are intact even after 700 cycles, further confirming the positive effect of the conformal TiO_2 coating, which ensured a high specific capacity at a high current density as well as long-term stability, as shown in Figs. 8 and 9.

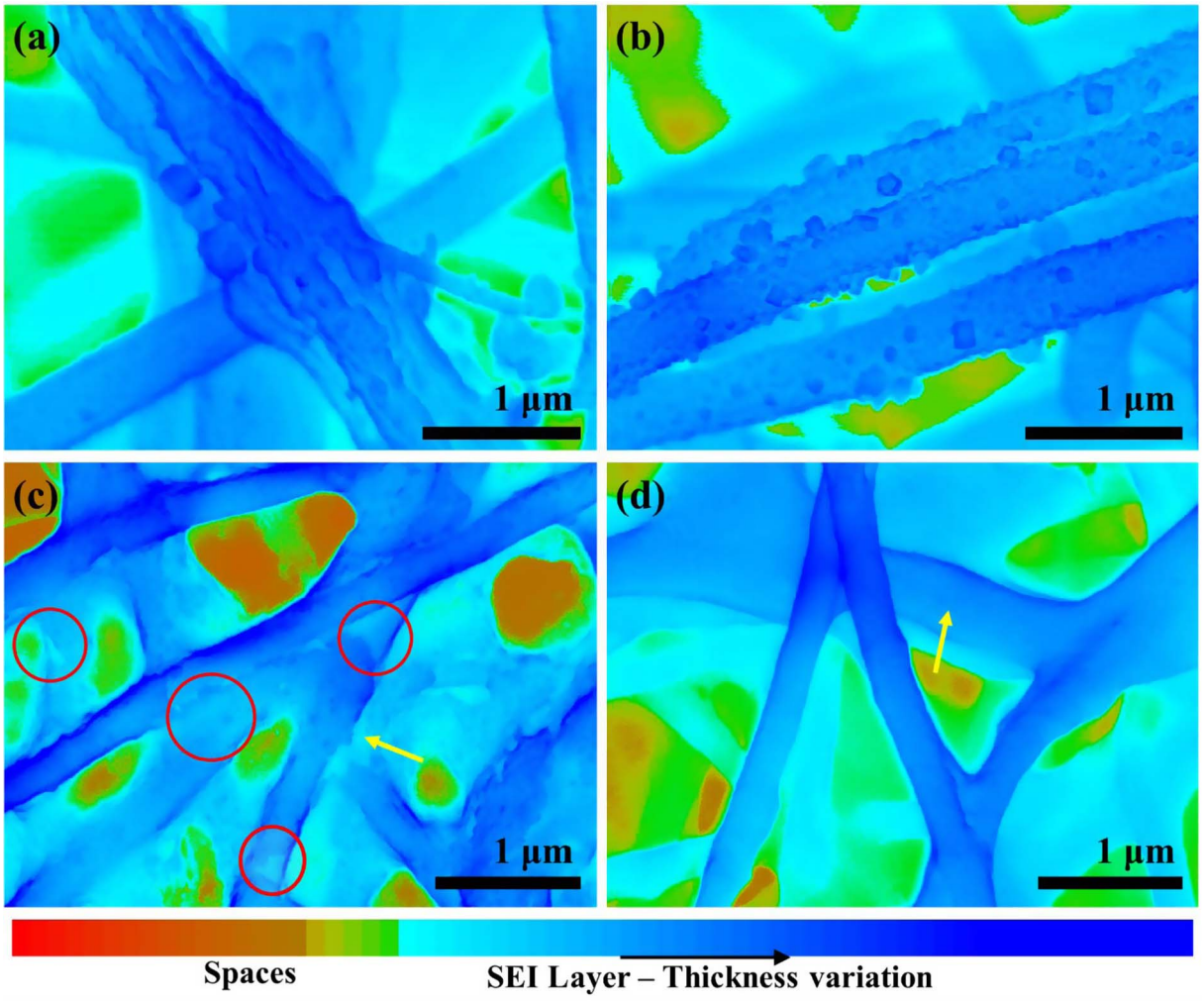

Fig. 11. SEM images of (a), (c) SZT0 and (b), (d) SZT50 after 2 and 700 cycles (images were processed in MATLAB to allow for improved visualization).

4. Conclusions

We demonstrated a low-cost and time-efficient technique for fabricating SnZnO/CNF composites coated with a thin passivating layer of TiO_2 using ALD. The freestanding, binder-free, and flexible SnZnO CNFs coated with TiO_2 exhibited excellent reversible capacity, which was as high as 413 $mAh{\cdot}g^{-1}$ at 5C. The composite CNFs also showed excellent long-term stability over 700 cycles. We found that the optimal number of ALD cycles for forming the TiO_2 coating was 50, as it resulted in composites that exhibited superior electrochemical performance. These results should promote the use of ALD in the battery industry for the development of durable and lightweight LIBs.

Acknowledgements

This research was supported by the Technology Development Program to Solve Climate Changes of the National Research Foundation (NRF) funded by the Ministry of Science, ICT & Future Planning (NRF-2016M1A2A2936760). This research was also supported by NRF-2013M3A6B1078879, NRF-2017R1A2B4005639, and MEST, 2016R1A2B3009481.

Appendix A. Supplementary data

Supplementary data associated with this article can be found, in the online version, at http://dx.doi.org/10.1016/j.cej.2018.01.004.

References

[1] B. Zhang, F. Kang, J.-M. Tarascon, J.-K. Kim, Progr. Mater. Sci. 76 (2016) 319–380.
[2] J.-W. Jung, C.-L. Lee, S. Yu, I.-D. Kim, J. Mater. Chem. A 4 (2016) 703–750.
[3] V.A. Agubra, D. De la Garza, L. Gallegos, M. Alcoutiabi, J. Appl. Polym. Sci. 42847 (2016) 42841–42848.
[4] E.S. Pampal, E. Stojanovska, B. Simon, A. Kilic, J. Power Sources 300 (2015) 199–215.
[5] V.A. Agubra, L. Zuniga, D. De la Garza, L. Gallegos, M. Pokhrel, M. Alcoutlabi, Solid State Ionics 286 (2016) 72–82.
[6] V.A. Agubra, L. Zuniga, D. Flores, H. Campos, J. Villarreal, M. Alcoutlabi, Electrochim. Acta 224 (2017) 608–621.
[7] I.M. Szilágyi, D. Nagy, J. Phys. Conf. Ser. 559 (2014) 012010.
[8] V.A. Agubra, L. Zuniga, D. Flores, J. Villareal, M. Alcoutlabi, Electrochim. Acta 192 (2016) 529–550.
[9] M. Usman Hameed, S. Ullah Dar, S. Ali, S. Liu, R. Akram, Z. Wu, I.S. Butler, Physica E 91 (2017) 119–127.
[10] Y. Deng, C. Fang, G. Chen, J. Power Sources 304 (2016) 81–101.
[11] B. Wang, B. Luo, X. Li, L. Zhi, Mater. Today 15 (2012) 544–552.
[12] S. Goriparti, E. Miele, F. De Angelis, E. Di Fabrizio, R. Proietti Zaccaria, C. Capiglia, J. Power Sources 257 (2014) 421–443.
[13] M. Yang, X. Li, B. Yan, L. Fan, Z. Yu, D. Li, J. Alloys Compd. 710 (2017) 323–330.
[14] X. Li, X. Li, L. Fan, Z. Yu, B. Yan, D. Xiong, X. Song, S. Li, K.R. Adair, D. Li, X. Sun, Appl. Surf. Sci. 412 (2017) 170–176.
[15] Y. Zhao, X. Li, L. Dong, B. Yan, H. Shan, D. Li, X. Sun, Int. J. Hydrogen Energy 40 (2015) 14338–14344.
[16] J. Liu, X. Sun, Nanotechnology 26 (2015) 024001.
[17] X.L. Huari Kou, Hui Shan, Linlin Fan, Bo Yan, Dejun Li, J. Mater. Chem. A 5 (2017) 17881–17888.
[18] D.C. Xinhui Xia, Chin Fan Ng, Jianyi Lin, Zhanxi Fan, Hua Zhang, Ze Xiang Shen, Hong Jin Fan, Mater. Horiz. 2 (2015) 237–244.
[19] L. Ma, R.B. Nuwayhid, T. Wu, Y. Lei, K. Amine, J. Lu, Adv. Mater. Interfaces 3 (2016) 1600564.
[20] X. Xia, Y. Wang, D. Wang, Y. Zhang, Z. Fan, J. Tu, H. Zhang, H.J. Fan, Nano Energy 20 (2016) 244–253.
[21] D. Guan, Y. Wang, Ionics 19 (2012) 1–8.
[22] H.-M. Cheng, F.-M. Wang, J.P. Chu, R. Santhanam, J. Rick, S.-C. Lo, J. Phys. Chem. C 116 (2012) 7629–7637.
[23] E. Kang, Y.S. Jung, A.S. Cavanagh, G.-H. Kim, S.M. George, A.C. Dillon, J.K. Kim, J. Lee, Adv. Funct. Mater. 21 (2011) 2430–2438.
[24] J. Li, X. Xiao, Y.-T. Cheng, M.W. Verbrugge, J. Phys. Chem. Lett. 4 (2013) 3387–3391.
[25] M. Li, X. Li, W. Li, X. Meng, Y. Yu, X. Sun, Electrochem. Commun. 57 (2015) 43–47.
[26] D. Wang, J. Yang, J. Liu, X. Li, R. Li, M. Cai, T.-K. Sham, X. Sun, J. Mater. Chem. A 2 (2014) 2306.
[27] C. Guan, J. Wang, Adv. Sci. (Weinh) 3 (2016) 1500405.
[28] N. Yesibolati, M. Shahid, W. Chen, M.N. Hedhili, M.C. Reuter, F.M. Ross, H.N. Alshareef, Small 10 (2014) 2849–2858.
[29] C. Guan, X. Wang, Q. Zhang, Z. Fan, H. Zhang, H.J. Fan, Nano Lett. 14 (2014) 4852–4858.
[30] Y. Bai, D. Yan, C. Yu, L. Cao, C. Wang, J. Zhang, H. Zhu, Y.-S. Hu, S. Dai, J. Lu, W. Zhang, J. Power Sources 308 (2016) 75–82.
[31] S. Licht, A. Douglas, J. Ren, R. Carter, M. Lefler, C.L. Pint, ACS Central Sci. 2 (2016) 162–168.
[32] N. Li, S.X. Jin, Q.Y. Liao, C.X. Wang, ACS Appl. Mater. Interfaces 6 (2014) 20590–20596.
[33] C. Guerra-Nunez, Y. Zhang, M. Li, V. Chawla, R. Erni, J. Michler, H.G. Park, I. Utke, Nanoscale 7 (2015) 10622–10633.
[34] S. Sengupta, A. Patra, M. Akhtar, K. Das, S.B. Majumder, S. Das, J. Alloys Compd. 705 (2017) 290–300.
[35] X.Y. Yu, H.B. Wu, L. Yu, F.X. Ma, X.W. Lou, Angew. Chem. Int. Ed. Engl. 54 (2015) 4001–4004.
[36] E. Samuel, H.S. Jo, B. Joshi, S. An, H.G. Park, Y. Il Kim, W.Y. Yoon, S.S. Yoon, Electrochim. Acta 231 (2017) 582–589.
[37] W. Wang, Z. Favors, C. Li, C. Liu, R. Ye, C. Fu, K. Bozhilov, J. Guo, M. Ozkan, C.S. Ozkan, Sci. Rep. 7 (2017) 44838.
[38] X. Liu, Q. Sun, A.M.C. Ng, A.B. Djurisic, M. Xie, B. Dai, J. Tang, C. Surya, C. Liao, K. Shih, RSC Adv. 5 (2015) 100783.